symmetry

MDPI

Article

Comparative Analysis of Darcy–Forchheimer Radiative Flow of a Water-Based Al_2O_3-Ag/TiO_2 Hybrid Nanofluid over a Riga Plate with Heat Sink/Source

R. Sindhu [1], Nazek Alessa [2], S. Eswaramoorthi [1] and Karuppusamy Loganathan [3,*]

1 Department of Mathematics, Dr. N.G.P. Arts and Science College, Coimbatore 641048, Tamil Nadu, India
2 Department of Mathematical Sciences, College of Sciences, Princess Nourah Bint Abdulrahman University, P.O. Box 84428, Riyadh 11671, Saudi Arabia
3 Department of Mathematics and Statistics, Manipal University Jaipur, Jaipur 303007, Rajasthan, India
* Correspondence: loganathankaruppusamy304@gmail.com

Abstract: The behavior of the Darcy–Forchheimer flow of a double-hybrid nanofluid toward a Riga plate with radiation and heat source/sink effects is investigated. The two different hybrid nanofluids, (Al_2O_3 and Ag) and (Al_2O_3 and TiO_2) with a base fluid (H_2O), are considered. The governing flow models with accompanying boundary constraints are reshaped into non-linear ODEs by applying the symmetry variables. The reshaped ODEs are numerically computed using Bvp4c in Matlab and the ND solver in Mathematica. The impact of the emerging parameters on the heat transfer, surface shear stress, temperature and velocity profile is scrutinized and expressed in a tabular and graphical structure. It is noticed that the upsurge of the Hartmann number leads to an improvement in the velocity profile. The velocity declines when enriching the porosity parameter. The radiation and Biot number lead to strengthening the temperature profile. The surface shear stress exalts due to a larger modified Hartman number. The radiation and unsteady parameters are downturns in the heat transfer gradient.

Keywords: Darcy–Forchheimer; hybrid nanofluid; heat sink/source; linear radiation; Riga plate; symmetry variables; suction/injection

check for updates

Citation: Sindhu, R.; Alessa, N.; Eswaramoorthi, S.; Loganathan, K. Comparative Analysis of Darcy–Forchheimer Radiative Flow of a Water-Based Al_2O_3-Ag/TiO_2 Hybrid Nanofluid over a Riga Plate with Heat Sink/Source. *Symmetry* **2023**, *15*, 199. https://doi.org/10.3390/sym15010199

Academic Editors: Calogero Vetro, Ranjit Kumar Upadhyay and Ramalingam Udhayakumar

Received: 14 December 2022
Revised: 27 December 2022
Accepted: 31 December 2022
Published: 9 January 2023

1. Introduction

Hybrid nanofluids are created by diffusing two different nanomaterials in the base fluid. Hybrid nanofluids outperform the nanofluids and base fluids in heat transfer efficiency. Hybrid nanofluid implementation has been significantly developed to improve the heat exchanger performance in various industrial and engineering procedures, organic and biological instruments and automobile heaters, see [1,2]. Hayat et al. [3] scrutinized the HT analysis of the Ag-CuO/H_2O HNF. Zainal et al. [4] studied the HT variations in an HNF over a permeable moving surface. They detected that the HT rate enriches when raising the NPVF. The impact of the Newtonian heating of a water-based Ag-Al_2O_3 HNF over an SS was studied. They found that the fluid friction rises due to an increase in the NPVF. The 2nd-order slip and heat absorption of the HNF in the porous medium was probed by Bakar et al. [5]. They demonstrated that the thermal transmission rate rises as the NPVF increases. Dadheech et al. [6] explored the MHD flow of the CuO-Ag/$C_2H_6O_2$ HNF over an SS. Their result shows that the velocity declines when the NPVF increases. The 3D MHD flow of an ethylene glycol-based HNF over an SS was inspected by Kumar et al. [7]. They noted that the solid VF leads to suppressing the transverse velocity field. Aladdin et al. [8] investigated the HT variations in a water-based Al_2O_3-TiO_2 HNF over a moving plate. They observed that the SFC rises when increasing the NPVF. Chahregh et al. [9] explained the Titanium-silver/blood hybrid nanofluid flow. They noted that the temperature gradient rises when there is an increased value of (ϕ_2). Devi and Devi [10] discussed the hybrid nanofluid Al_2O_3-Cu/H_2O and Cu/H_2O nanofluid over an SS. They observed that the VF (ϕ_2) grows in the temperature gradient, alternatively reducing the velocity gradient. Ali et al. [11] analyzed the HT on Carboxymethyl cellulose/H_2O across a hybrid nanofluid. They noted that the drag friction and the LN grow when enhancing the NPVF.

The fluid movement throughout a porous material is crucial in many contexts, including crude oil production, nuclear waste documents, grain amassing, thermal isolation and many more. A famous phrase for describing the qualities of a substance in a porous medium was coined by Darcy. However, he failed to account for boundary and inertia effects. Porous media uses in today's era of lightning-fast technology fall into distinct categories based on their respective speeds. When this occurs, the flow is irregular. Because this is the case, inertia and boundary features must be taken into account. This restriction was lifted by Forchheimer [12], who modified the Darcian equation to include a square velocity term. For more significant Reynolds numbers, this expression holds, and it was later given the name the "Forchheimer term". Haider et al. [13] explored the flow of an HNF through a Darcy–Forchheimer medium. They discovered that the porosity parameter improves the SFC. Khan et al. [14] probed the DF flow of a water-based HNF with a Marangon convection. They observed that a growing porosity parameter leads to a decrease in the fluid velocity. The entropy optimization of a DF flow of an HNF on an SS was analyzed by Khan et al. [15]. They noted that the local Nusselt number decreases as the porosity parameter increases. The 3D DF and radiative flow of glycerin-based CNTs past a Riga plate with the Cattaneo–Christov theory were analytically investigated by Eswaramoorthi et al. [16]. They detected that the Forchheimer strongly affects skin friction. Tayyab et al. [17] evaluated the changes in a 3D MHD DF flow of the nanofluid with a dissipation impact. They proved that the concentration profile upgrades when upgrading the Forchheimer number.

The outputs of a heat source/sink become a crucial component in many different industrial processes, such as semiconductors, transistors, the storage of foodstuffs, packed bed reactors, optoelectronic devices and air conditioning, amongst others. Alzahrani et al. [18] explored the consequences of an MHD DF flow of an HNF past a flat plate with a heat source/sink. Their results clearly show that the heat source/sink parameter improves the thermal profile. The impact of a heat source/sink of 2D time-dependent water/kerosene-based carbon nanotubes past a heated Riga plate was demonstrated by Prabakaran et al. [19]. It is seen from this study that the nanoliquid temperature grows with a larger heat source/sink parameter. Mumraiz et al. [20] used the Adams–Bashforth procedure to solve the problem of an MHD HNF past an SS with a non-linear heat sink/source. They revealed that the nanofluid temperature grows when improving the heat source parameter. The radiative MHD flow of a nanofluid past an uneven inclined shrinking/stretching sheet with a heat source/sink was presented by Thumma et al. [21]. They proved that the heat source/sink cases upgrade the heat transfer gradient values. Mabood et al. [22] probed the consequences of a non-uniform heat sink/source of an MHD flow of thermally radiative micropolar fluid over an SS. They demonstrated that the fluid temperature decays when developing the heat sink/source parameter. The impact of a space/thermal-dependent heat source of an MHD nanofluid in a rotating disk was inspected by Mahanthesh et al. [23]. They proved that the space-dependent heat source parameter leads to developing the nanofluid temperature. Ramandevi et al. [24] evaluated the MHD flow of a Casson/viscoelastic fluid past an SS with a non-uniform heat sink/source effect. They noticed the thicker thermic boundary layer attained in the Casson fluid compared to the viscoelastic fluid for a varying space-dependent heat sink/source parameter.

The electrodes are alternatively built on the Riga plate, which is hydromagnetic induced in the presence of a fluid flow. The Riga plate's innovative composition and placement in various fluid flow models are crucial in causing the Lorentz effect to have an impact. Gailitis and Lielausis [25], who conducted this research experimentally in the Riga Laboratory, were the ones who initially proposed this advanced Riga plate mechanism. Several fluid flow issues are solved by the Riga plate configuration, which is very useful and successful. For example, in many physical settings, especially in submarines, the design helps reduce skin friction. Fluid dynamics and other biological processes employ the Riga plate in various ways. The primary determinant in the Riga plate's magnetic term cast-off is known as the Hartmann number, and in such a scenario, fluid motion is considered. Ahmed et al. [26] probed the nanofluid flow through a Riga plate. The 3D flow of the Casson/Williamson nanofluid past a Riga plate was investigated by Akolade et al. [27]. They observed that the nanofluid concentration decreases when enriching the Hartman number. The radiative flow of a nanofluid past a Riga plate was explored by Kumar et al. [28]. They observed that the nanofluid temperature decreases when enhancing the Hartman number. Adeosun et al. [29] analyzed the flow of a Casson nanofluid on a heated stretching Riga plate. They made the discovery that when they improved the modified Hartmann number, the local Sherwood number also improved. Numerical research on entropy optimization of the time-dependent Oldroyd-B nanofluid over the Riga plate was conducted by Mburu et al. [30]. They found that the Harman number leads to a rise in the entropy generation.

To the best of the authors' knowledge, as shown by the analysis above, no efforts have been taken to scrutinize the impact of a DF flow of a water-based Ag-Al_2O_3 and TiO_2-Al_2O_3 HNF with the influence of radiation and a non-uniform heat sink/source past a heated Riga plate. The flow that is caused by thermal radiation plays a vital role in polymer preparation, gas turbines, furnace design, nuclear reactor cooling, thermal insulation and many others. We rest assured that our computational outcomes are implemented in any real-time problems in various areas of thermal engineering, heating/cooling processes, energy generation, the design of new thermal systems, etc. The current investigation aims to find answers to the following research issues:

- What are the unique rheological characteristics of water-based Ag-Al_2O_3 and TiO_2-Al_2O_3 hybrid nanofluids?
- What is the impact of the Darcy–Forchheimer flow over a Riga plate?
- How do thermal radiation and the non-uniform heat sink/source phenomena impact the heat transfer?
- What is the significance of the slip effect in the velocity profile?
- How is the heat transfer process made by applying the convective heating condition?

2. Mathematical Formulation

Consider the steady 2D DF flow of HNF toward a Riga plate. Let the x-axis run parallel to the plate and the y-axis run perpendicular to it. The flow is maintained in the direction of $y \leq 0$ toward a plate. Let us consider that the temperature of the fluid, denoted by T_w, is higher than the temperature of the surrounding environment, marked by T_∞. The thermal radiation and non-uniform heat sink/source effects are considered. It is expected that the sheet's surface will be heated convectively by a hot fluid with a temperature of T_f and this makes a heat exchange coefficient h_c. The schematic layout of the dual type of HNF and structure of the Riga plate are plotted in Figure 1a,b. The rheological equation of the governing flow models is expressed as follows, see Sulochana et al. [31]:

$$\frac{\partial u}{\partial x} + \frac{\partial v}{\partial y} = 0, \tag{1}$$

$$u\frac{\partial u}{\partial x} + v\frac{\partial u}{\partial y} = \frac{\mu_{hnf}}{\rho_{hnf}}\frac{\partial^2 u}{\partial y^2} - \frac{\nu_{hnf}}{k_1}u - \frac{c_b}{x\sqrt{k^{**}}}u^2 - \frac{\pi J_0 M_0}{8\rho}exp(-\frac{\pi}{a_1}y), \tag{2}$$

$$\begin{aligned} u\frac{\partial T}{\partial x} + v\frac{\partial T}{\partial y} = {} & \frac{K_{hnf}}{(\rho c_p)_{hnf}}\left(\frac{\partial^2 T}{\partial y^2}\right) + \frac{16\sigma^* T^3}{3k^*(\rho c_p)_{hnf}}\left(\frac{\partial^2 T}{\partial y^2}\right) + \frac{q^{***}}{(\rho c_p)_{hnf}}\Big[A(T_f - T_\infty)f' \\ & + B(T - T_\infty)\Big], \end{aligned} \tag{3}$$

where

$$q^{***} = \frac{k_{hnf} U_w}{x \nu_{hnf}}$$

The corresponding boundary conditions are

$$u = U_w + \mu_{hnf} L_1, \;\; v = -V_w, \;\; -k_{hnf} \frac{\partial T}{\partial y} = h_c [T_f - T] \;\; \text{at} \;\; y = 0 \tag{4}$$

$$u \to 0, \;\; v \to 0; \;\; T \to T_\infty \;\; \text{as} \;\; y \to 0 \tag{5}$$

Define the symmetry variables

$$u = cxf^{'}(\eta), \;\; v = -\sqrt{cv_f} f(\eta), \;\; \eta = \sqrt{\frac{c}{\nu_f}} y, \;\; \theta = \frac{T - T_\infty}{T_f - T_\infty} \tag{6}$$

Using the above symmetry variables (6) into Equations (2) and (3),

$$\frac{1}{A_1 A_2} f^{'''}(\eta) + f(\eta) f^{''}(\eta) - f^{'2}(\eta) - Fr f^{'2}(\eta) + Ha e^{-\beta\eta} - \lambda f^{'}(\eta) \frac{1}{A_1 A_2} = 0, \tag{7}$$

$$\left[\frac{A_5}{A_3}\frac{1}{Pr} + \frac{4}{3} Rd \frac{1}{Pr}\frac{1}{A_3}\right]\theta^{''}(\eta) + \frac{A_5}{A_3}\frac{1}{Pr} A_1 A_2 \left[A f^{'}(\eta) + B\theta(\eta)\right] + f(\eta)\theta^{'}(\eta) = 0, \tag{8}$$

subject to the boundary condition

$$f(0) = fw; \;\; f^{'}(0) = \left(1 + \frac{K}{A_1}\right) f''(0); \;\; f'(\infty) = 0;$$

$$\theta'(0) = -[1 - \theta(0)] \frac{Bi}{A_5}; \;\; \theta(\infty) = 0 \tag{9}$$

where

$$A_1 = (1 - \phi_1)^{2.5} (1 - \phi_2)^{2.5};$$

$$A_2 = (1 - \phi_2)\left((1 - \phi_1) + \phi_1 \left(\frac{\rho_1}{\rho_f}\right)\right) + \phi_2 \left(\frac{\rho_2}{\rho_f}\right);$$

$$A_3 = (1 - \phi_2)\left((1 - \phi_1) + \phi_1 \left(\frac{\rho_1 c_{\rho 1}}{\rho_f c_{\rho_f}}\right)\right) + \phi_2 \left(\frac{\rho_2 c_{\rho 2}}{\rho_f c_{\rho_f}}\right);$$

$$A_4 = k_f \left(\frac{k_1 + (z-1)k_f - (z-1)\phi_1 (k_f - k_1)}{k_1 + (z-1)k_f + \phi_1 (k_f - k_1)}\right);$$

$$A_5 = \left(\frac{k_1 + (z-1)k_f - (z-1)\phi_1 (k_f - k_1)}{k_1 + (z-1)k_f + \phi_1 (k_f - k_1)}\right)\left(\frac{k_2 + (z-1)A_4 - (z-1)\phi_2 (A_4 - k_2)}{k_2 + (z-1)A_4 + \phi_2 (A_4 - k_2)}\right);$$

For this purpose, the skin friction coefficient and the reduced local Nusselt number are the relevant physical quantities, which are defined as follows:

$$\frac{1}{2} C_f \sqrt{Re} = \frac{f^{''}(0)}{A_1}; \;\; \frac{Nu}{\sqrt{Re}} = -\left(A_5 + \frac{4}{3} Rd\right)\theta'(0)$$

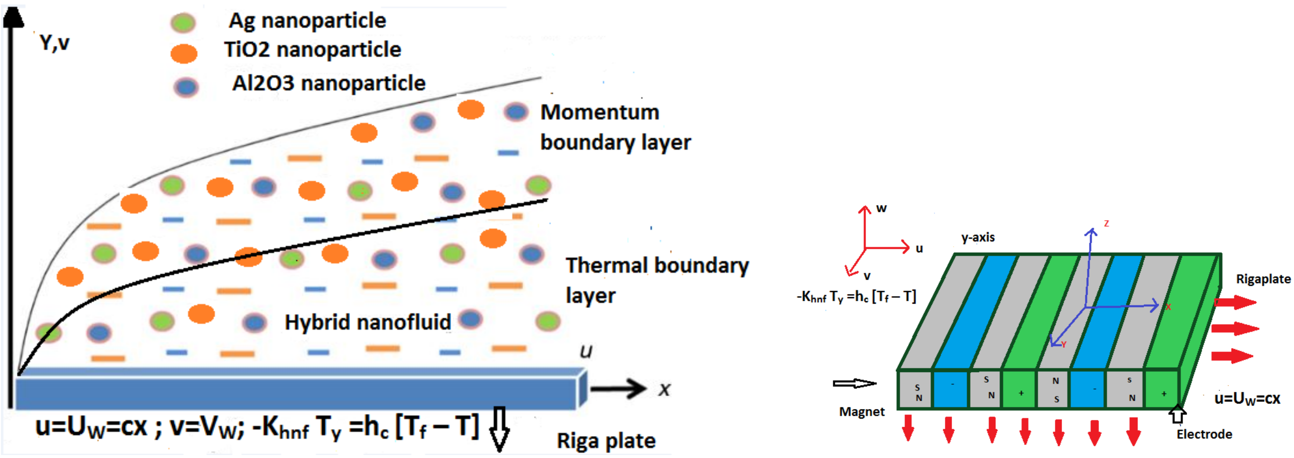

(a) **(b)**

Figure 1. The schematic layout of the flow model (**a**) and the structure of the Riga plate (**b**).

3. Methodology

3.1. Bvp4c Scheme

The Bvp4c approach is used to numerically solve dimensionless (7) and (8) using a specified boundary condition (9), see Abbas et al. [32]. Let us take
$f = s_1, f' = s_2, f'' = s_3, f''' = s_3', \theta = s_4, \theta' = s_5, \theta'' = s_5'$.

The equations in the system are

$$
\begin{aligned}
s_1' &= s_2\\
s_2' &= s_3\\
s_3' &= A_1A_2\left((s_2)^2 - s_1s_3 + Frs_2{}^2 + Ha\frac{1}{A_2}Exp(-\beta\eta) - \lambda s_2\frac{1}{A_1A_2}\right)\\
s_4' &= s_5\\
s_5' &= \frac{-s_1s_5 - \frac{A_1A_2A_5}{A_3}\frac{1}{Pr}[As_2 + Bs_4]}{\frac{A_5}{A_3}\frac{1}{Pr} + \frac{4}{3}Rd\frac{1}{Pr}\frac{1}{A_3}}
\end{aligned}
$$

As a result, the boundary conditions in Equation (9) are

$$
s_1(0) = fw,\;\; s_2(0) = \left(1 + \frac{K}{A_1}\right)s_3(0),\;\; s_4(0) = 0,\;\; s_5(\infty) = [1 - s_4(0)]\frac{-Bi}{A_5}[1-\theta(0)],\;\; s_4(\infty) = 0
$$

As the point at which convergence must be achieved, the number 10^{-5} was decided upon with step size of 0.05.

3.2. ND Solver

The reduced models (7) and (8) with the condition (9) are solved by applying ND solver.

$$
\begin{aligned}
&Equation1 = NDSolve\Bigg[\Bigg\{\frac{1}{A_1A_2}f'''(\eta) + \Big(f(\eta)f''(\eta) - (f')^2(\eta) - Fr(f')^2(\eta)\Big) + Ha e^{-\beta\eta} - \lambda f'\frac{1}{A_1A_2} == 0,\\
&\left[\frac{A_5}{A_3}\frac{1}{Pr} + \frac{4}{3}Rd\frac{1}{Pr}\frac{1}{A_3}\right]\theta''(\eta) + \frac{A_5}{A_3}\frac{1}{Pr}A_1A_2\left[Af' + B\theta\right] + f\theta' == 0,\\
&f(0) = fw;\;\; f'(0) = \left(1 + \frac{K}{A_1}\right)f''(0);\;\; f'(\infty) = 0;\;\; \theta'(0) = -[1-\theta(0)]\frac{Bi}{A_5};\;\; \theta(\infty) = 0\Bigg\}, \{f,\theta\}, \{\eta, 0, 12\}\Bigg];\\
&Evaluate[f[\eta]/.Equation1];\\
&Evaluate[\theta[\eta]/.Equation1];
\end{aligned}
$$

4. Results and Discussion

This section provides the effects of the relevant flow factors on the velocity, temperature, SFC and LNN with a constant magnitude of the Prandtl number. The thermophysical properties of a conventional and HNF are compiled in Tables 1 and 2. Table 3 explains the comparison of the previous and present results and found that our computational results exactly matched with Ibrahim and Shankar [33]. Table 4 shows the estimate of Ha, λ, Fr, fw, ϕ_1 and ϕ_2 on the SFC. The SFC increases when the modified Hartmann number increases. On the other hand, the SFC slows down to improve the quality of λ, Fr, fw, ϕ_1 and ϕ_2. It is noticed that the SFC for (Ag and Al_2O_3) is high when compared to (TiO_2 and Al_2O_3). Table 5 summarizes the effects of Rd, A, B, Bi, K and Bi on the LNN. It is observed that the LNN enhances when it slumps the values of Rd, A, B and K.

Figure 2a–d demonstrate the impact of λ, fr, fw and Ha on the velocity field. It is observed that the fluid speed decreases as it increases the λ, Fr and fw. However, it develops when heightening the modified Harmann number. In physics, a more extensive modification of the Hartman number produces a stronger field, producing a more substantial wall parallel to a Lorentz force. As a result, the fluid speed increases. The size of the porosity parameter (λ) tends to increase the fluid resistance during the flow, resulting in a halving of the speed and a reduction in the thickness of the MBL. Furthermore, it was noted that the MBL thickness is higher in the (Ag-Al_2O_3) nanoparticle than in the (TiO_2-Al_2O_3) nanoparticle. The NPVF ϕ_1 and ϕ_2 on the velocity profile is portrayed in Figure 3a,b. It is noticed that the fluid speed decreases near the plate, and it enhances the plate far away when escalating the values of ϕ_1. The more presence of ϕ_2 decays the fluid velocity profile. Figure 4a–d portray the temperature variations in A, B, Rd and K. It is discovered that the fluid warmness increases when enlarging the values of A, B and Rd, and it slumps for large size of K. Physically, the most significant quantity of the radiation parameter develops the transport energy level of the fluid. Thus, the fluid hotness improves. The fluid thermal field is reduced with the slip parameter's increasing value. Physically, the slip parameter makes the flow strike over the surface. By increasing the heat source and sink parameters, the maximum temperature inside the liquid is generated, which increases the thickness of the TBL, and this causes an improvement in the fluid thermal field.

The temperature distributions of fw, Bi, ϕ_1 and ϕ_2 are sketched in Figure 5a–d. It is observed that the fluid temperature heightens as it strengthens the values of Bi, ϕ_1 and ϕ_2, and the reverse trend is obtained for the suction/injection parameter. Physically, the greater the convective heating parameter's ($Bi \geq 0$) magnitude, the richer the HT coefficient, increasing the fluid heat and thickening the thermal barrier layer. Additionally, it should be highlighted that the TiO_2-Al_2O_3 nanoparticle has a thicker thermal boundary layer than the Ag-Al_2O_3 nanoparticle. Physically, the Ag-Al_2O_3/H_2O nanoparticles have a higher thermal conductivity than the TiO_2-Al_2O_3/H_2O nanoparticles. The effect of λ, fw, Fr and Ha on the SFC for both cases is shown in Figure 6a,b. This graph demonstrates that increasing the values of λ, fw and Fr decays the surface shear stress. However, a greater presence of Ha leads to improving the surface shear stress. The local Nusselt number for different values of fw, B, Bi and Rd for both cases are plotted in Figure 7a,b. It can be seen that the HTR decreases when enhancing the values of B and it increases when there are greater values of fw, Bi and Rd. In addition, the HTG is lesser in TiO_2-Al_2O_3/H_2O than the Ag-Al_2O_3/H_2O.

Figure 8a–d display the decimating percentage of the surface shear stress for various Ha, Λ, Fr and fw values in the Ag-Al_2O_3/H_2O HNF, TiO_2-Al_2O_3/H_2O HNF and viscous fluid. The maximum decimating percentage of the SFC is Ag-Al_2O_3 (8.12%), TiO_2-Al_2O_3 (6.8%) and viscous fluid (9.74%), attained when the Ha changes from 0.5 to 0.7. The minimum decimating percentage of the SFC is Ag-Al_2O_3 (3.86%), TiO_2-Al_2O_3 (3.32) and viscous fluid (4.7%), attained when the Ha changes from 0 to 0.3. The maximum decimating percentage of the SFC is Ag-Al_2O_3 (3.18%), TiO_2-Al_2O_3 (2.33%) and viscous fluid (2.90%), attained when the L changes from 0.1 to 0.2. The minimum decimating percentage of the SFC is Ag-Al_2O_3 (2.88%), TiO_2-Al_2O_3 (1.77) and viscous fluid (2.18%), attained when the L changes from 0.4 to 0.5. The maximum decimating percentage of the SFC is Ag-Al_2O_3 (8.30%), TiO_2-Al_2O_3 (7.44%) and viscous fluid (10.96%), attained when the Fr changes from 3 to 4. The minimum decimating percentage of the SFC is Ag-Al_2O_3 (2.61%), TiO_2-Al_2O_3 (2.44) and viscous fluid (3.72%), attained when the Fr changes from 3 to 4. The maximum decimating percentage of the SFC is Ag-Al_2O_3 (2.05%), TiO_2-Al_2O_3 (2.28%) and viscous fluid (2.59%), attained when the fw changes from -0.2 to -0.1. The minimum decimating percentage of the SFC is Ag-Al_2O_3 (2.03%), TiO_2-Al_2O_3 (2.27) and viscous fluid (2.58%), attained when the fw changes from 0.1 to 0.2.

Figure 9a–d show the percentage increase in the wall shear stress for different Bi, Rd, A and B values in Ag-Al_2O_3/H_2O, TiO_2-Al_2O_3/H_2O and viscous fluid. The maximum increasing percentage of the LNN is Ag-Al_2O_3 (13.07%), TiO_2-Al_2O_3 (13.48%) and viscous fluid (17.50%), attained when the Rd changes from 0.2 to 0.4. The minimum increasing percentage of the LNN is Ag-Al_2O_3 (8.68%), TiO_2-Al_2O_3 (8.79) and viscous fluid (10.05%), attained when the Rd changes from 0.8 to 1. The maximum increasing percentage of the LNN is Ag-Al_2O_3 (5.48%), TiO_2-Al_2O_3 (6.57%) and viscous fluid (4.73%), attained when the A changes from 0 to 0.4. The minimum increasing percentage of the LNN is Ag-Al_2O_3 (6.56%), TiO_2-Al_2O_3 (8.19) and viscous fluid (2.76%), attained when the A changes from 0.8 to 1.2. The maximum increasing percentage of the LNN is Ag-Al_2O_3 (0.81%), TiO_2-Al_2O_3 (1.35%) and viscous fluid (0.79%), attained when the B changes from 0.6 to 0.8. The minimum increasing percentage of the LNN is Ag-Al_2O_3 (0.59%), TiO_2-Al_2O_3 (0.87) and viscous fluid (0.59%), attained when the B changes from 0 to 0.2. The maximum increasing percentage of the LNN is Ag-Al_2O_3 (176.30%), TiO_2-Al_2O_3 (15.1%) and viscous fluid (171.75%), attained when the Bi changes from 0.1 to 0.3. The minimum increasing percentage of the LNN is Ag-Al_2O_3 (29.59%), TiO_2-Al_2O_3 (29.10) and viscous fluid (27.68%), attained when the Bi changes from 0.7 to 1.

Table 1. Ag and TiO_2 thermal properties along with Al_2O_3 and H_2O, see Yaseen et al. [34].

Physical Properties	Fluid Phase (H_2O)	Silver (Ag)	Titanium Dioxide (TiO_2)	Aluminum Oxide (Al_2O_3)
ρ (kg/m^3)	997.1	235	4250	3970
c_p (J/kg K)	4179	10,500	686.2	765
k (W/mk)	0.613	429	8.9538	40
σ (s/m)	5.5×10^{-6}	6.30×10^{-7}	2.6×10^{6}	35×10^{6}

Table 2. Thermophysical properties of hybrid nanofluid.

Properties	Hybrid Nanofluid
Density	$\rho_{hnf} = (1-\phi_2)[(1-\phi_1)\rho_f + \phi_1\rho_{s1}] + \phi_2(\rho c_p)_{s2}$
Heat capacity	$(\rho c_p)_{hnf} = (1-\phi_2)[(1-\phi_1)(\rho c_p)_f + \phi 1(\rho c_p)_{s1}] + \phi_2(\rho c_p)_{s2}$
Viscosity	$\mu_{hnf} = \frac{\mu_f}{(1-\phi_1)^{2.5}((1-\phi_2)^{2.5}}$
Thermal conductivity	$\frac{k_{hnf}}{k_{bf}} = \frac{k_{s2}+(n-1)k_{bf}-(n-1)\phi_2(k_{bf}-k_{s2})}{k_{s2}+(n-1)k_{bf}+\phi_2(k_{bf}-k_{s2})}$ where $\frac{k_{bf}}{k_f} = \frac{k_{s1}+(n-1)k_f-(n-1)\phi_1(k_f-k_{s1})}{k_{s1}+(n-1)k_f+\phi_1(k_f-k_{s1})}$
Electrical conductivity	$\frac{\sigma_{hnf}}{\sigma_{bf}} = \frac{\sigma_{s2}+2\sigma_{bf}-2\phi_2(\sigma_{bf}-\sigma_{s2})}{\sigma_{s2}+2\sigma_{bf}+\phi_2(\sigma_{bf}-\sigma_{s2})}$
	$\frac{\sigma_{bf}}{\sigma_f} = \frac{\sigma_{s1}+2\sigma_{bf}-2\phi_1(\sigma_{bf}-\sigma_{s1})}{\sigma_{s1}+2\sigma_{bf}+\phi_1(\sigma_1-\sigma_{s1})}$

Table 3. Comparison of $-f''(0)$ for distinct values of fw with $\lambda = \phi_1 = \phi_2 = Fr = Ha = K = 0$ to Ibrahim and Shankar [33].

fw	Present Study		Ref. [33]
	Bvp4c	ND Solver	
0	1.00000	1.00001	1.0000
0.5	1.28078	1.28078	1.2808

Table 4. The skin friction coefficient forAg-Al_2O_3/H_2O and TiO_2-Al_2O_3/H_2O HNFs.

		Ag-Al_2O_3/H_2O	**Ag-Al_2O_3/H_2O**	**TiO_2-Al_2O_3/H_2O**	**TiO_2-Al_2O_3/H_2O**
		Bvp4c	***NDSolver***	***Bvp4c***	***NDSolver***
Ha	0	−0.562711	−0.562711	−0.595213	−0.595213
	0.1	−0.540986	−0.540986	−0.575445	−0.575445
	0.3	−0.499511	−0.499511	−0.537887	−0.537887
	0.5	−0.460255	−0.460255	−0.502515	−0.502515
	0.7	−0.422850	−0.422850	−0.468935	−0.468935
λ	0.1	−0.499511	−0.499511	−0.537887	−0.537887
	0.2	−0.515399	−0.515399	−0.550468	−0.550468
	0.3	−0.530011	−0.530011	−0.562181	−0.562181
	0.4	−0.543476	−0.543476	−0.573100	−0.573100
	0.5	−0.555911	−0.555911	−0.583294	−0.583294
Fr	0	−0.481630	−0.481630	−0.520502	−0.520502
	1	−0.521646	−0.521646	−0.559266	−0.559266
	2	−0.550264	−0.550264	−0.586692	−0.583294
	3	−0.572290	−0.572290	−0.607649	−0.604906
fw	−0.2	−0.434850	−0.443461	−0.464807	−0.464807
	−0.1	−0.443765	−0.445879	−0.475397	−0.475397
	0	−0.452860	−0.455008	−0.486241	−0.486241
	0.1	−0.462119	−0.464288	−0.497313	−0.497313
	0.2	−0.471525	−0.473703	−0.508582	−0.508582
ϕ_1	0.1	−0.492861	−0.490702	−0.531567	−0.531567
	0.2	−0.516085	−0.516085	−0.585404	−0.584773
	0.3	−0.551503	−0.551503	−0.636758	−0.636758
	0.4	−0.601836	−0.601836	−0.688535	−0.688535
	0.5	−0.672610	−0.672610	−0.744083	−0.744083
ϕ_2	0.005	−0.466898	−0.466898	−0.513836	−0.513836
	0.02	−0.479422	−0.479422	−0.521495	−0.521495
	0.04	−0.492861	−0.492861	−0.531567	−0.531567
	0.06	−0.505892	−0.505892	−0.541496	−0.541496

Table 5. The local Nusslet number for Ag-Al_2O_3/water and TiO_2-Al_2O_3/water HNFs.

		Ag-Al_2O_3/H_2O	**Ag-Al_2O_3/H_2O**	**TiO_2-Al_2O_3/H_2O**	**TiO_2-Al_2O_3/H_2O**
		Bvp4c	***NDSolver***	***Bvp4c***	***NDSolver***
Rd	0.2	0.641494	0.641494	0.646670	0.646670
	0.4	0.629771	0.629771	0.633556	0.633556
	0.6	0.618767	0.618767	0.621242	0.621242
	0.8	0.608384	0.608384	0.609626	0.609626
	1	0.598548	0.598548	0.598618	0.598618
A	0	0.652317	0.652317	0.659596	0.659596
	0.4	0.609026	0.609026	0.607891	0.607891
	0.8	0.565736	0.565736	0.556185	0.556185
	1.2	0.522445	0.522445	0.504480	0.504480
	1.6	0.479154	0.479154	0.452775	0.452775
B	0	0.644516	0.644516	0.651085	0.651085
	0.2	0.641494	0.641494	0.646670	0.646670
	0.4	0.638207	0.638207	0.641699	0.641699
	0.6	0.634618	0.634618	0.636043	0.636043
	0.8	0.630673	0.630673	0.629530	0.629530

Table 5. *Cont.*

		$Ag\text{-}Al_2O_3/H_2O$	$Ag\text{-}Al_2O_3/H_2O$	$TiO_2\text{-}Al_2O_3/H_2O$	$TiO_2\text{-}Al_2O_3/H_2O$
		Bvp4c	***NDSolver***	***Bvp4c***	***NDSolver***
K	0	0.636282	0.636282	0.640946	0.640946
	0.5	0.624810	0.624810	0.627977	0.627977
	1	0.619472	0.619472	0.622350	0.622350
	1.5	0.616187	0.616187	0.618978	0.618978
	2	0.613918	0.613918	0.616687	0.616687
Bi	0.1	0.145151	0.145151	0.146942	0.146942
	0.3	0.401049	0.401049	0.404327	0.404327
	0.5	0.619472	0.619472	0.622350	0.622350
	0.7	0.808091	0.808091	0.809399	0.809399
	1	1.047241	1.047240	1.044945	1.044950

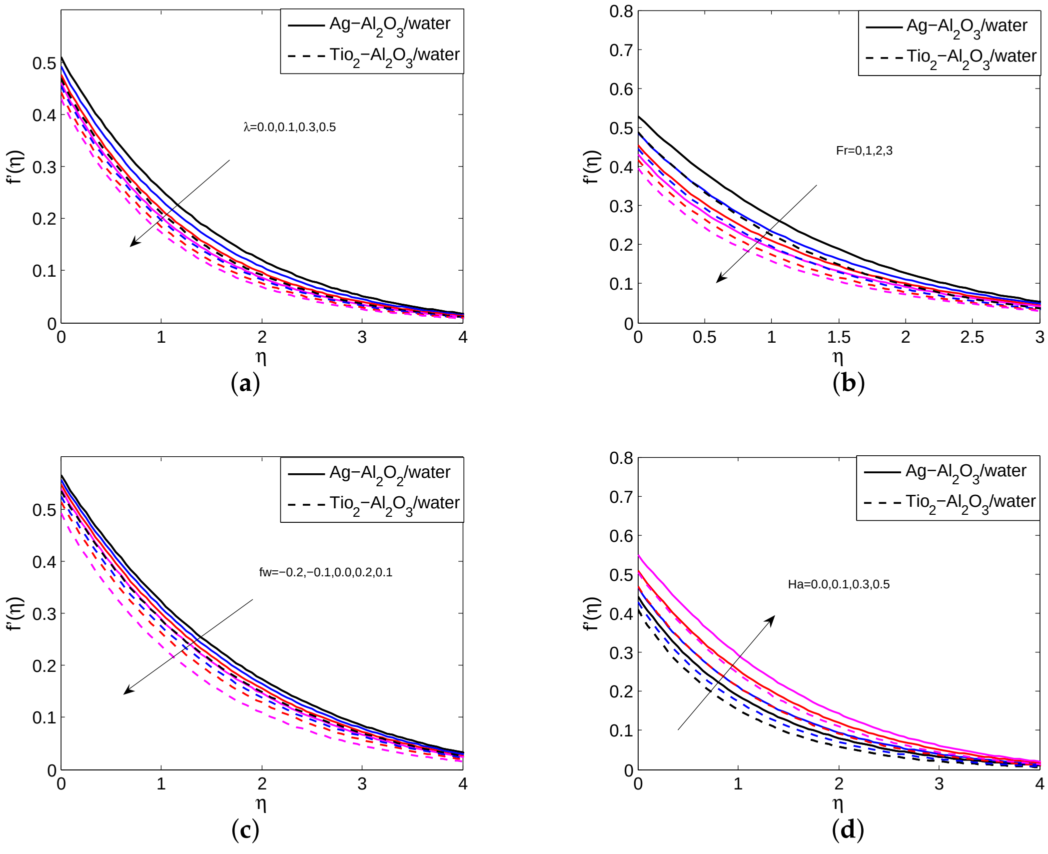

Figure 2. The velocity profile for various values of (**a**) λ, (**b**) Fr, (**c**) fw, (**d**) Ha.

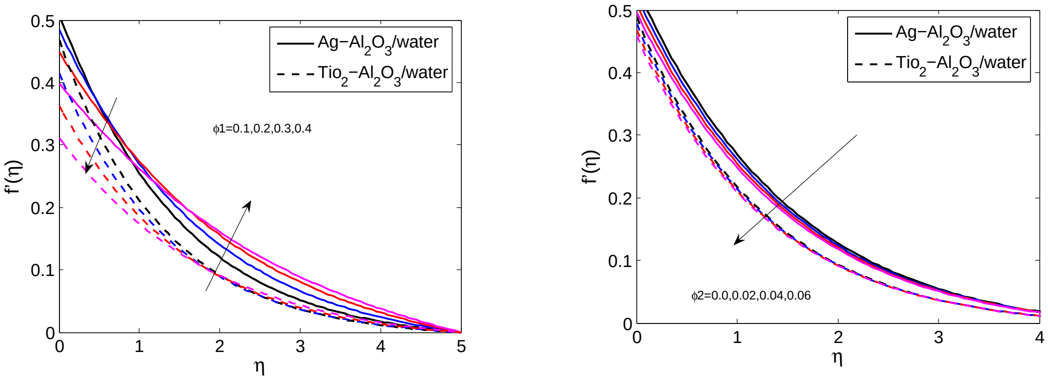

(**a**) (**b**)

Figure 3. The velocity profile for various values of (**a**) ϕ_1, (**b**) ϕ_2.

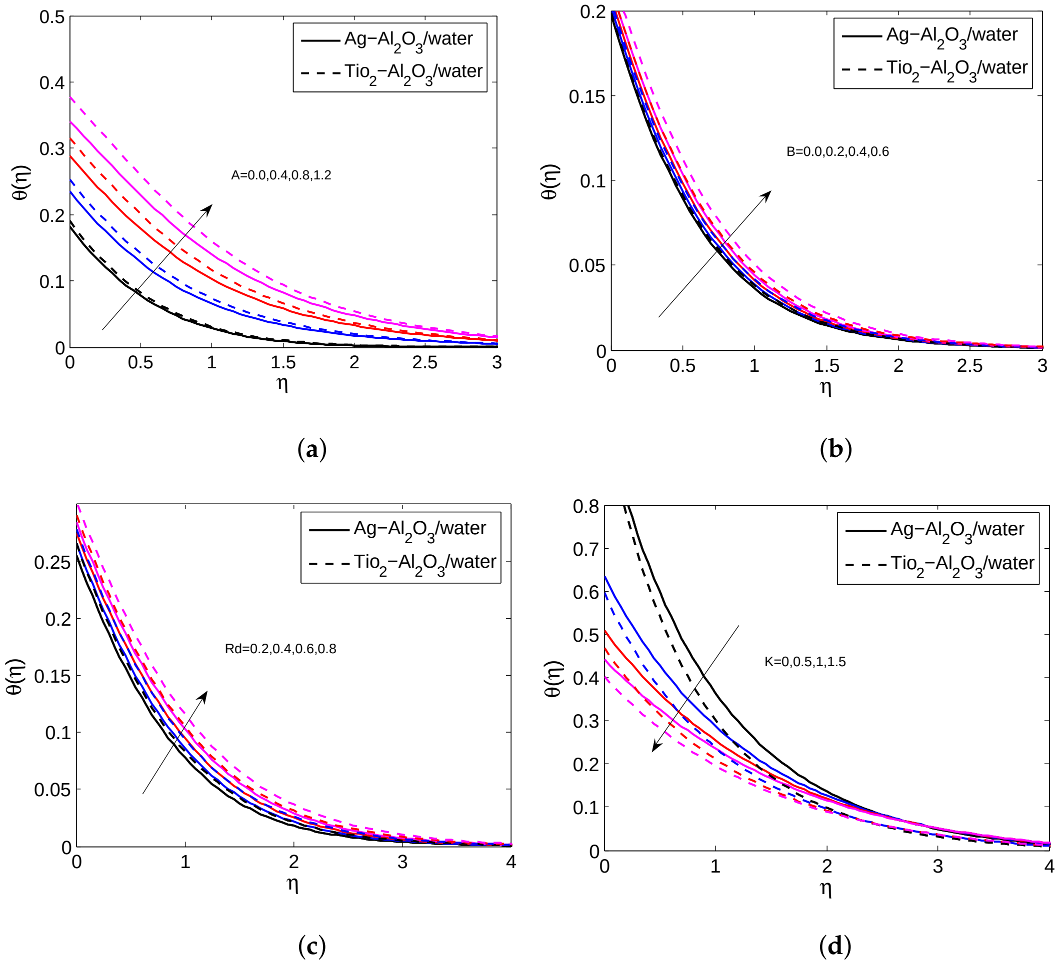

(**a**) (**b**)

(**c**) (**d**)

Figure 4. The temperature profile for various values of (**a**) A, (**b**) B, (**c**) Rd, (**d**) K.

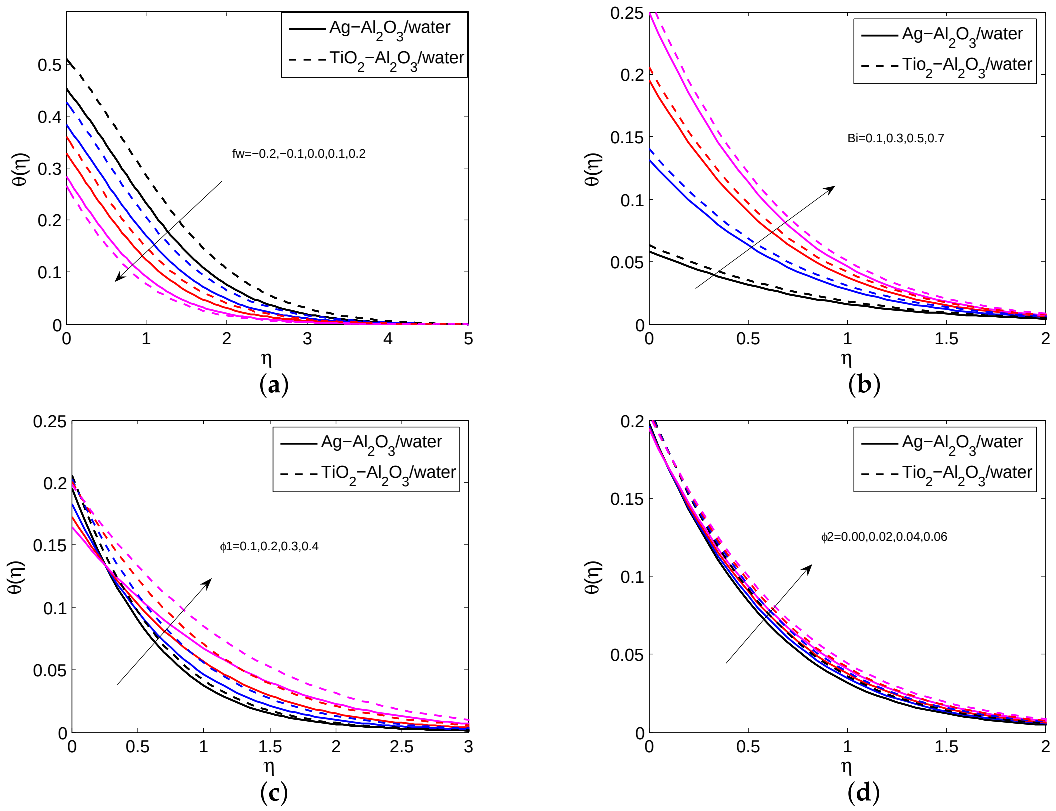

Figure 5. The temperature profile for various values of (**a**) fw, (**b**) Bi, (**c**) ϕ_1, (**d**) ϕ_2.

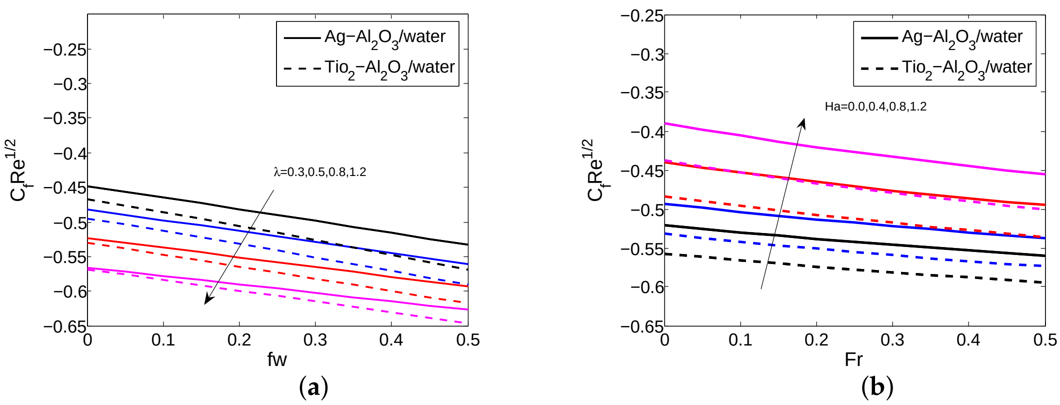

Figure 6. The skin friction coefficient for different combination of λ, Fr, fw and Ha.

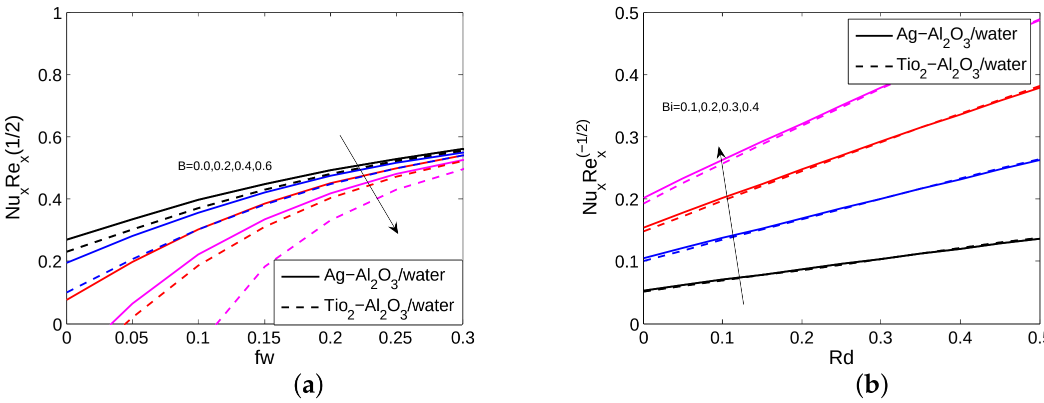

Figure 7. The local Nusselt number for different combination of fw, B, Rd and Bi.

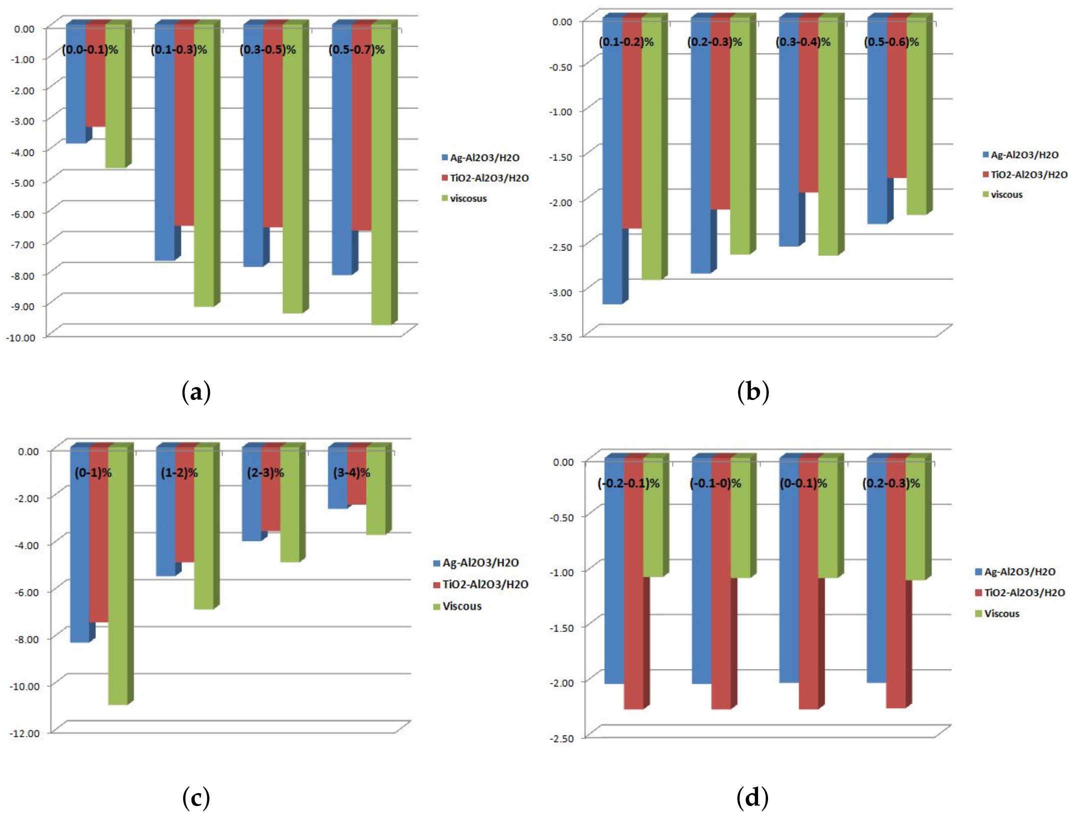

Figure 8. The improving/decimating percentage of skin friction coefficient for different values of (**a**) Ha, (**b**) λ, (**c**) Fr, (**d**) fw.

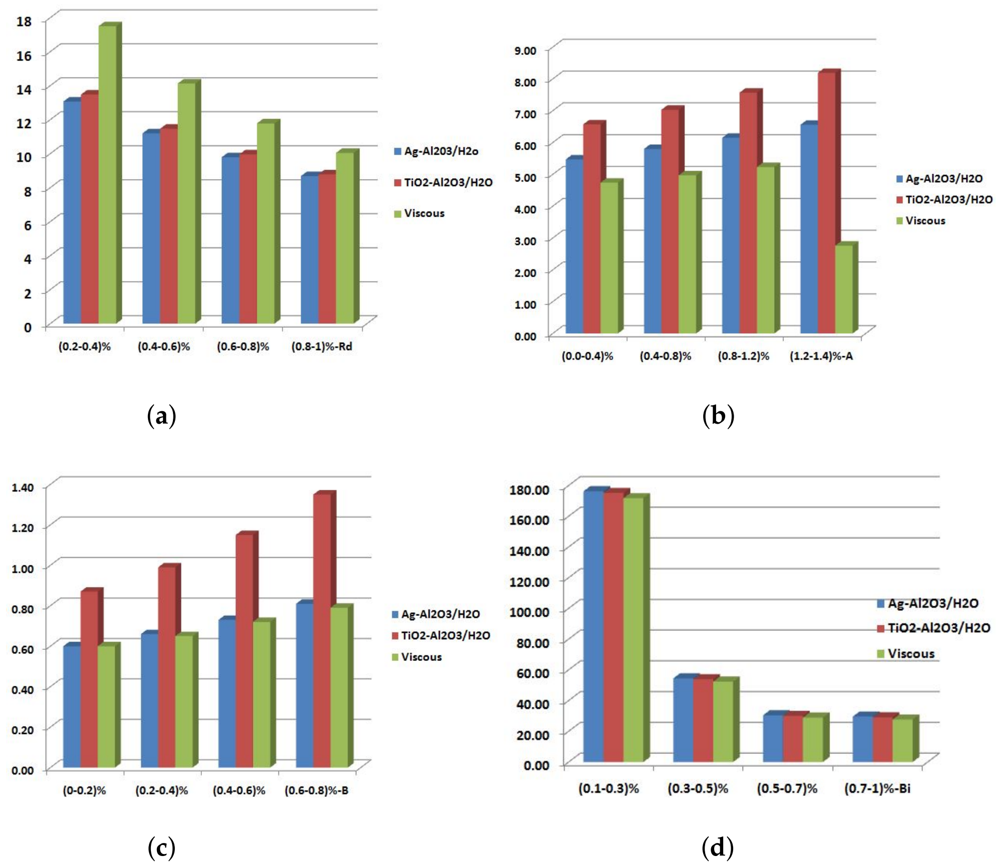

Figure 9. The improving/decimating percentage of local Nusselt number for different values of (**a**) Rd, (**b**) A, (**c**) B, (**d**) Bi.

5. Conclusions

The current work scrutinizes the consequences of the thermal radiation of a Darcy–Forchheimer flow of a H_2O-based Ag-TiO_2/Al_2O_3 hybrid nanofluid over a Riga plate with a heat sink/source and suction/injection. The suitable symmetry variables are used to remodel the governing problems into ODE models, and these resulting models are solved numerically by the Bvp4c technique and ND solver. The main findings are as follows:

- The fluid velocity downturns when upturning the porosity parameter, Forchheimer number and injection/suction parameter
- The momentum boundary layer thickness is higher in the Ag-Al_2O_3 hybrid nanofluid than the TiO_2/Al_2O_3 hybrid nanofluid.
- The radiation, space and temperature-dependent parameters lead to reinforcing the thermal boundary layer.
- The skin friction coefficient reduces for a greater quantity of the porosity parameter and Forchheimer number.
- The Biot number and radiation parameter develop the local Nusselt number.
- The skin friction coefficient and local Nusselt number are higher in the Ag-Al_2O_3 hybrid nanofluid than the TiO_2/Al_2O_3 hybrid nanofluid.

Author Contributions: Conceptualization, S.E. and K.L.; methodology, S.E.; software, K.L.; validation, S.E., N.A. and K.L.; formal analysis, R.S. and S.E.; investigation, N.A.; resources, K.L.; data curation, N.A.; writing-original draft preparation, R.S. and S.E.; writing—review and editing, K.L. and S.E.; visualization, S.E.; supervision, K.L.; project administration, N.A.; funding acquisition, N.A. All authors have read and agreed to the published version of the manuscript.

Funding: Princess Nourah Bint Abdulrahman University Researchers Supporting Project number (PNURSP2023R59), Princess Nourah Bint Abdulrahman University, Riyadh, Saudi Arabia.

Data Availability Statement: Not applicable.

Acknowledgments: We appreciate Princess Nourah Bint Abdulrahman University Researchers Supporting Project number (PNURSP2023R59), Princess Nourah Bint Abdulrahman University, Riyadh, Saudi Arabia.

Conflicts of Interest: The authors declare no conflict of interest.

Nomenclature

Symbols	**Description**
J_0	applied current density of the electrodes
x,y	Cartesian coordinates (m)
θ	dimensionless temperature
c_b	drag coefficient
h_c	heat transfer coefficient
M_0	magnetization of the permanent magnets
a_1	magnets positioned in the interval separating the electrodes
$\frac{Nu}{R}e^{(}-1/2)$	Nusselt number
k_1	permeability of the porous medium
T_w	surface temperature (K)
τ_w	surface shear stress
U_w, V_w	surface stretching velocities $(m^2 s^{-1})$
fw	suction/injection parameter
σ^*	Stefen–Boltzmann coefficient
K	slip parameter
c_p	specific heat capacity
A	space-dependent coefficient
$C_f Re^{1/2}$	skin friction coefficient
T_f	temperature of the hot fluid (K)
T	temperature of the fluid (K)
k^*	thermal conductivity (K)
T_∞	temperature away from the sheet (K)
B	temperature-dependent coefficient (K)
u,v	velocity components
Bi	Biot number
$\beta\left(=\frac{\pi}{a_1}\sqrt{\frac{\nu_f}{c}}\right)$	dimensionless parameter
$Fr\left(=\frac{c_b}{\sqrt{k_1^*}}\right)$	Forchheimer number
$\Gamma(=\frac{T_f}{T_\infty})$	heating variable
$Ha\left(=\frac{\pi J_0 M_0}{8\rho_f c^2 x}\right)$	modified Hartmann number
$\lambda\left(=\frac{\nu_f}{k^* c}\right)$	porosity parameter
$Pr\left(=\frac{(\mu c_p)_f}{k_f}\right)$	Prandtl number
$Rd\left(=\frac{4\sigma T_\infty^3}{k^* k_f}\right)$	radiation parameter
Greek symbols	
ρ	density
η	dimensionless variable
ρ_{nf}	density of nanofluid
ρ_{hnf}	density of hybrid nanofluid
μ_{hnf}	hybrid nanofluid viscosity
ν	kinematic viscosity
μ_{nf}	nanofluid viscosity
μ	viscosity
Abbreviation	
CNTs	carbon nanotubes
HTG	heat transfer gradient
HNF	hybrid nanofluid

HT	heat transfer
HTR	heat transfer rate
LNN	local Nusselt number
MHD	magnetohydrodynamics
MBL	momentum boundary layer
$NPVF$	nanoparticle volume friction
SFC	skin friction coefficient
SS	stretching sheet
TBL	thermal boundary layer

References

1. Jamil, F.; Ali, H.M. Applications of hybrid nanofluids in different fields. In *Hybrid Nanofluids for Convection Heat Transfer*; Academic Press: Cambridge, MA, USA, 2020; pp. 215–254.
2. Muneeshwaran, M.; Srinivasan, G.; Muthukumar, P.; Wang, C.C. Role of hybrid-nanofluid in heat transfer enhancement-A review. *Int. Commun. Heat Mass Transf.* **2021**, *125*, 105341. [CrossRef]
3. Hayat, T.; Nadeem, S. Heat transfer enhancement with Ag-CuO/water hybrid nanofluid. *Results Phys.* **2017**, *7*, 2317–2324. [CrossRef]
4. Zainal, N.A.; Nazar, R.; Naganthran, K.; Pop, I. MHD flow and heat transfer of hybrid nanofluid over a permeable moving surface in the presence of thermal radiation. *Int. J. Heat Fluid Flow* **2020**, *31*, 858–879. [CrossRef]
5. Bakar, S.A.; Arifin, N.M.; Bachok, N.; Ali, F.M. Hybrid Nanofluid Flow in a Porous Medium with Second-Order Velocity Slip, Suction and Heat Absorption. *Malaysian J. Math. Sci.* **2022**, *16*, 257–272. [CrossRef]
6. Dadheech, P.K.; Agrawal, P.; Purohit, S.D.; Kumar, D. Study of Flow and Heat Transfer of CuO-Ag/$C_2H_6O_2$ Hybrid Nanofluid over a Stretching Surface with Porous Media and MHD Effect. *Sci. Technol. Asia* **2021**, *26*, 174–181.
7. Kumar, T.S. Hybrid nanofluid slip flow and heat transfer over a stretching surface. *Partial. Differ. Equ. Appl. Math.* **2021**, *4*, 100070. [CrossRef]
8. Aladdin, N.A.L.; Bachok, N. Boundary layer flow and heat transfer of Al_2O_3-TiO_2/water hybrid nanofluid over a permeable moving plate. *Symmetry* **2020**, *12*, 1064. [CrossRef]
9. Chahregh, H.S.; Dinarvand, S. TiO_2-Ag/blood hybrid nanofluid flow through an artery with applications of drug delivery and blood circulation in the respiratory system. *Int. J. Numer. Methods Heat Fluid Flow* **2020**, *30*, 4775–4796. [CrossRef]
10. Devi, S.A.; Devi, S.S.U. Numerical investigation of hydromagnetic hybrid CuI_2O_3/water nanofluid flow over a permeable stretching sheet with suction. *Int. J. Nonlinear Sci. Numer. Simul.* **2016**, *17*, 249–257. [CrossRef]
11. Ali, F.; Loganathan, K.; Eswaramoorthi, S.; Prabu, K.; Zaib, A.; Chaudhary, D.K. Heat Transfer Analysis on Carboxymethyl Cellulose Water-Based Cross Hybrid Nanofluid Flow with Entropy Generation. *J. Nanomater.* **2022**, *2022*, 5252918. [CrossRef]
12. Forchheimer, P. Wasserbewegung durch boden. *Z. Ver. Deutsch. Ing.* **1901**, *45*, 1782–1788.
13. Haider, F.; Hayat, T.; Alsaedi, A. Flow of hybrid nanofluid through Darcy-Forchheimer porous space with variable characteristics. *Alex. Eng. J.* **2021**, *60*, 3047–3056. [CrossRef]
14. Khan, M.I.; Qayyum, S.; Shah, F.; Kumar, R.N.; Gowda, R.P.; Prasannakumara, B.C.; Chu, Y.M.; Kadry, S. Marangoni convective flow of hybrid nanofluid ($MnZnFe_2O_4$-$NiZnFe_2O_4$-H_2O) with Darcy Forchheimer medium. *Ain Shams Eng. J.* **2021**, *12*, 3931–3938. [CrossRef]
15. Khan, S.A.; Khan, M.I.; Hayat, T.; Alsaedi, A. Darcy-Forchheimer hybrid (MoS_2, SiO_2) nanofluid flow with entropy generation. *Comput. Methods Programs Biomed.* **2020**, *185*, 105152. [CrossRef] [PubMed]
16. Eswaramoorthi, S.; Loganathan, K.; Reema, J.; Gyeltshen, S. Darcy-Forchheimer 3D Flow of Glycerin-Based Carbon Nanotubes on a Riga Plate with Nonlinear Thermal Radiation and Cattaneo-Christov Heat Flux. *J. Nanomater.* **2022**, *2022*, 5286921. [CrossRef]
17. Tayyab, M.; Siddique, I.; Jarad, F.; Ashraf, M.K.; Ali, B. Numerical solution of 3D rotating nanofluid flow subject to Darcy-Forchheimer law, bio-convection and activation energy. *S. Afr. J. Chem. Eng.* **2022**, *40*, 48–56. [CrossRef]
18. Alzahrani, A.K.; Ullah, M.Z.; Alshomrani, A.S.; Gul, T. Hybrid nanofluid flow in a Darcy-Forchheimer permeable medium over a flat plate due to solar radiation. *Case Stud. Therm. Eng.* **2021**, *26*, 100955. [CrossRef]
19. Prabakaran, R.; Eswaramoorthi, S.; Loganathan, K.; Gyeltshen, S. Thermal Radiation and Viscous Dissipation Impacts of Water and Kerosene-Based Carbon Nanotubes over a Heated Riga Sheet. *J. Nanomater.* **2022**, *2022*, 1865763. [CrossRef]
20. Mumraiz, S.; Ali, A.; Awais, M.; Shutaywi, M.; Shah, Z. Entropy generation in electrical magnetohydrodynamic flow of Al_2O_3-Cu/H_2O hybrid nanofluid with non-uniform heat flux. *J. Therm. Anal. Calorim.* **2020**, *143*, 14. [CrossRef]
21. Thumma, T.; Beg, O.A.; Kadir, A. Numerical study of heat source/sink effects on dissipative magnetic nanofluid flow from a non-linear inclined stretching/shrinking sheet. *J. Mol. Liq.* **2017**, *232*, 159–173. [CrossRef]
22. Mabood, F.; Ibrahim, S.M.; Rashidi, M.M.; Shadloo, M.S.; Lorenzini, G. Non-uniform heat source/sink and Soret effects on MHD non-Darcian convective flow past a stretching sheet in a micropolar fluid with radiation. *Int. J. Heat Mass Transf.* **2016**, *93*, 674-682. [CrossRef]
23. Mahanthesh, B.; Lorenzini, G.; Oudina, F.M.; Animasaun, I.L. Significance of exponential space- and thermal-dependent heat source effects on nanofluid flow due to radially elongated disk with Coriolis and Lorentz forces. *J. Therm. Anal. Calorim.* **2019**, *141*, 37–44. [CrossRef]

24. Ramandevi, B.; Reddy, J.V.R.; Sugunamma, V.; Sandeep, N. Combined influence of viscous dissipation and non-uniform heat source/sink on MHD non-Newtonian fluid with Cattaneo–Christov heat flux. *Alex. Eng. J.* **2018**, 57, 1009–1018. [CrossRef]
25. Gailitis, A.; Lielausis, O. On the possibility to reduce the hydrodynamic drag of a plate in an electrolyte. *Appl. Magnetohydrodyn. Rep. Inst. Phys. Riga* **1961**, *13*, 143–146.
26. Ahmad, A.; Asghar, S.; Afzal, S. Flow of nanofluid past a Riga plate. *J. Magn. Magn. Mater.* **2016**, *402*, 44–48. [CrossRef]
27. Akolade, M.T.; Tijani, Y.O. A comparative study of three dimensional flow of Casson–Williamson nanofluids past a riga plate: Spectral quasi-linearization approach. *Partial. Differ. Equ. Appl. Math.* **2021**, *4*, 100108. [CrossRef]
28. Kumar, R.; Sood, S.; Shehzad, S.A.; Sheikholeslami, M. Radiative heat transfer study for flow of non-Newtonian nanofluid past a Riga plate with variable thickness. *J. Mol. Liq.* **2017**, *248*, 143–152. [CrossRef]
29. Adeosun, A.T.; Gbadeyan, J.A.; Lebelo, R.S. Heat transport of Casson nanofluid flow over a melting Riga plate embedded in a porous medium. *Int. J. Eng. Res. Afr.* **2021**, *55*, 15–27. [CrossRef]
30. Mburu, Z.M.; Mondal, S.; Sibanda, P.; Sharma, R. A numerical study of entropy generation on Oldroyd-B nanofluid flow past a riga plate. *J. Therm. Eng.* **2021**, *7*, 845–866. [CrossRef]
31. Sulochana, C.; Kumar, T.P.; Uma, M.S.; Thulasi, L. MHD Darcy-Forchheimer hybrid nanofluid flow past a nonlinear stretching surface:Numerical study. *IOP Conf. Ser. Mater. Sci. Eng.* **2021**, *1145*, 012042. [CrossRef]
32. Abbas, N.; Shatanawi, W.; Abodayeh, K. Computational analysis of MHD nonlinear radiation casson hybrid nanofluid flow at vertical stretching sheet. *Symmetry* **2022**, *14*, 1494. [CrossRef]
33. Ibrahim, W.; Shankar, B. MHD boundary layer flow and heat transfer of a nanofluid past a permeable stretching sheet with velocity, thermal and solutal slip boundary conditions. *Comput. Fluids* **2013**, *75*, 1–10. [CrossRef]
34. Yaseen, M.; Rawat, S.K.; Shafiq, A.; Kumar, M.; Nonlaopon, K. Analysis of heat transfer of mono and hybrid nanofluid flow between two parallel plates in a Darcy porous medium with thermal radiation and heat generation/absorption. *Symmetry* **2022**, *14*, 1943. [CrossRef]